Redox Biology 70 (2024) 103050

Contents lists available at ScienceDirect

Redox Biology

journal homepage: www.elsevier.com/locate/redox

Guiding bar motif of thioredoxin reductase 1 modulates enzymatic activity and inhibitor binding by communicating with the co-factor FAD and regulating the flexible C-terminal redox motif

Wuyang Shi [a,2], Shibo Sun [a,2], Haowen Liu [a,2], Yao Meng [a], Kangshuai Ren [a], Guoying Wang [a], Minghui Liu [a], Jiaqi Wu [a,1], Yue Zhang [a], Huang Huang [a], Meiyun Shi [a], Weiping Xu [b], Qiang Ma [c], Bingbing Sun [d], Jianqiang Xu [a,*]

[a] *School of Life and Pharmaceutical Sciences (LPS) & Panjin Institute of Industrial Technology (PIIT), Dalian University of Technology, Panjin, 124221, China*
[b] *School of Ocean Science and Technology (OST) & Key Laboratory of Industrial Ecology and Environmental Engineering (Ministry of Education), Dalian University of Technology, Panjin, 124221, China*
[c] *Chinese Academy of Inspection and Quarantine, Beijing, 100176, China*
[d] *State Key Laboratory of Fine Chemicals, School of Chemical Engineering (CE), Dalian University of Technology, Dalian, 116023, China*

ARTICLE INFO

Keywords:
Thioredoxin reductase
Thioredoxin
Selenoprotein
Guiding bar motif
Caveolin-1
LCS3

ABSTRACT

Thioredoxin reductase (TXNRD) is a selenoprotein that plays a crucial role in cellular antioxidant defense. Previously, a distinctive guiding bar motif was identified in TXNRD1, which influences the transfer of electrons. In this study, utilizing single amino acid substitution and Excitation-Emission Matrix (EEM) fluorescence spectrum analysis, we discovered that the guiding bar communicates with the FAD and modulates the electron flow of the enzyme. Differential Scanning Fluorimetry (DSF) analysis demonstrated that the aromatic amino acid in guiding bar is a stabilizer for TXNRD1. Kinetic analysis revealed that the guiding bar is vital for the disulfide reductase activity but hinders the selenocysteine-independent reduction activity of TXNRD1. Meanwhile, the guiding bar shields the selenocysteine residue of TXNRD1 from the attack of electrophilic reagents. We also found that the inhibition of TXNRD1 by caveolin-1 scaffolding domain (CSD) peptides and compound LCS3 did not bind to the guiding bar motif. In summary, the obtained results highlight new aspects of the guiding bar that restrict the flexibility of the C-terminal redox motif and govern the transition from antioxidant to pro-oxidant.

1. Introduction

Mammalian selenoprotein thioredoxin reductase 1 (TXNRD1), belonging to the pyridine nucleotide disulfide oxidoreductase family, is primarily responsible for restoring the reduced states of thioredoxin (TXN) and thioredoxin-related protein of 14 kDa (TRP14) [1]. The TXN system supports several fundamental biological processes, such as facilitating DNA synthesis, repairing oxidative damage to proteins, and quenching excessive reactive oxygen species (ROS) in cell [2,3]. TXNRD1 contains an N-terminal glutathione reductase (GSR)-like redox motif, which comprises two catalytic residues Cys^{59} and Cys^{64}, and a C-terminal selenium (Se)-containing redox motif, with additional redox-active residues Cys^{497} and Sec^{498}. The C-terminus is generally flexible and redox-active, and has been described as the “catalytic tail” of the enzyme [4].

During the catalysis of TXNRD1, a non-covalently bound co-factor FAD is first converted to its reduced form $FADH_2$ by accepting two electrons from NADPH. $FADH_2$ is able to form a charge-transfer complex (CTC) with the Cys^{64} residue, and these two states are classified as the two-electron-reduced enzymes (EH_2). With the addition of the second reducing equivalent, the redox motif located at the C-terminal was reduced, resulting in the conversion of the enzyme to a four-electron-reduced enzyme (EH_4) [4]. Upon the reduction of TXN, the EH_4 enzyme undergoes oxidation, resulting in the formation of EH_2 form. Briefly, the general electron flow is: NADPH→FAD→CVNVGC→GCUG→TXN1 (or TRP14 and TXNL1) [5–7].

---

[*] Corresponding author.
E-mail address: jianqiang.xu@dlut.edu.cn (J. Xu).
[1] Shanghai Key Laboratory of Metabolic Remodeling and Health, Institute of Metabolism and Integrative Biology, Fudan University, Shanghai, 200433, China.
[2] These authors contributed equally to this study.

https://doi.org/10.1016/j.redox.2024.103050
Received 12 November 2023; Received in revised form 5 January 2024; Accepted 17 January 2024

In addition to these physiological substrates, other low-weight compounds, such as pyrroloquinoline quinone (PQQ) [8], toxoflavin [9], and coenzyme Q10 [10], have been identified as efficient substrates of TXNRD1.

The “guiding bar” motif of TXNRD, formed by Trp^{407}, Asn^{418}, and Asn^{419}, was first conceptualized by Katja Becker’s group [11,12]. The unique motif plays a vital role in guiding the movement of the catalytic tail of TXNRD1 towards substrates by interacting with residues 494–496 at the C-terminus [11,12]. Site-directed mutations of the motif increased the catalytic efficiency of Sec-deficient TXNRD1 variants in both thioredoxin reducing and DTNB reducing [12]. Moreover, Hondal and his colleagues reported that the rearrangement of C-terminal tail, guided by the guiding bar, is the primary mechanistic difference between cytosolic TXNRD1 and mitochondrial TXNRD2 [13]. The presence of the motif in TXNRD1 may govern the interaction between the oxidized C-terminal redox center and the N-terminal redox center, thus facilitating redox cycling, which emphasizes the significant dependence of TXNRD1 on selenium [14]. The guiding bar limits the access of other substrates to the N-terminus. As a result, the selenium atom must function as both an electron acceptor from the N-terminal redox center and an electron donor to substrates [14]. The replacement of Sec with Cys must account for the reduced reactivity of both nucleophilicity of the selenol in donating electrons and electrophilicity in thiol/disulfide exchange, resulting in a significant decrease in catalytic activity [15–19].

The hypothesis of the guiding bar motif introduces innovative insights for several unresolved questions related to TXNRD1, such as the formation and function of selenium-compromised thioredoxin reductase-derived apoptotic proteins (SecTRAPs) [20,21], the rationale behind the high efficiency exhibited by the Sec-to-Cys mutant of TXNRD1 in juglone and shikonin reduction [22,23], and the mechanism of the resistance of TXNRD2 to electrophilic compounds [24]. To our knowledge, solid evidence supporting the function of guiding bar in TXNRD1 catalysis remains elusive. Meanwhile, the role of the highly conserved motif in other crucial enzymes in relation to redox regulation remains unclear to date.

In this study, recombinant rat TXNRD1 and its variants with mutations in the guiding bar motif were employed to perform side-by-side biochemical comparisons, aiming to elucidate the role of the guiding bar motif in TXNRD1. The UV–vis wavelength scanning and Excitation-Emission Matrix (EEM) fluorescence spectrum analysis of mutant variants indicated that the guiding bar communicates with the FAD and is involved in the electron transfer process of the selenoenzyme. Mutating the residues of guiding bar increases the catalytic efficiency of TXNRD1 in the reduction of juglone. Notably, the TXNRD1 variants were more susceptible to electrophilic reagents and exhibited increased production of superoxide ions from SecTRAPs. The results obtained in this study provide valuable insights into the catalytic mechanism of TXNRD1 and demonstrate that the unique guiding bar motif functions as a gearbox for tuning the flexible C-terminal tail and adjusting TXNRD1 catalysis.

2. Results

2.1. Sequence alignment of TXNRD1 from different species reveals that guiding bars are conserved

Generally, TXNRD1 is a homodimeric enzyme, with two subunits forming a head-to-tail assembly [4,5]. To catalyze substrates, the enzyme requires the movement of the C-terminal tail from a close position to the N-terminal motif of the other subunit toward the substrates [5]. The overall structure of TXNRD1’s catalytic pocket reveals that the guiding bar motif is located parallel to the C-terminal tail (Fig. 1A and B). To verify the conservation of the motif in TXNRD1, we conducted a partial sequence alignment of selected mammalian TXNRD1 (Fig. 1C and Fig. S1). Trp^{407}, Asn^{418}, and Asn^{419}, which are core residues in the guiding bar motif, are highly conserved in mammalian TXNRD1. Notably, we observed that the motif is abundant in aromatic residues, such as Tyr^{402}, Phe^{405}, Phe^{406}, Trp^{407}, and Trp^{411} in rat TXNRD1 (Fig. 1C and Fig. S1). Given the crucial role of aromatic amino acids in stabilizing protein structure [25] and facilitating electron transfer [26,27], it is imperative to uncover the physiological function of this motif in TXNRD1.

2.2. Mutating key residues in guiding bar disaffects the reducibility of C-terminal tail in TXNRD1

To investigate the unique motif in TXNRD1, we generated a series of constructs (Fig. S2), with either single amino acid residue mutations or multiple residue substitutions on the core residues and the adjacent aromatic residues in the guiding bar motif (Primer list in Table S1). For subsequent analysis, we employed recombinant rat TXNRD1 and its mutants, given the enhanced stability of rat TXNRD1 compared to human TXNRD1 [24,28]. Furthermore, rat TXNRD1 is commonly utilized in TXNRD1 related enzymatic studies, and an overall sequences alignment revealed a high homology between the rat and human TXNRD1 (Fig. S3). The TXNRD1 variants were produced in *E. coli* BL21 (DE3) *gor*$^{-}$ cells, co-expressing with the bacterial SECIS element for selenocysteine insertion [29,30]. SDS-PAGE analysis clearly showed a strong band with a molecular weight (MW) of 55 kDa, corresponding to the subunit of TXNRD1 (Fig. 1D). Given the guiding bar motif was reported to regulate the movement of the C-terminal tail of TXNRD1 [11], we initially examined whether the selenocysteine residue of the mutant variants can be reduced and further labeled by 5-IAF. In contrast to oxidized forms of TXNRD1, NADPH-pre-reduced TXNRD1 variants, including W407A and N418A/N419A mutants, can be labeled by 5-IAF (Fig. 1E), indicating that the C-terminal selenolthiol of the TXNRD1 variants with mutations at the guiding bar motif is functional to be reduced by NADPH through the reductive half-reaction.

2.3. Guiding bar of TXNRD1 interacts with the co-factor FAD and impacts the electron flow of the enzyme

The spectrum of UV–Vis for all TXNRD1 variants displays a typical peak at 463 nm, which represents the non-covalently bound FAD (Fig. 1F, Fig. S4). Meanwhile, TXNRD1 variants exhibit a characteristic absorbance shoulder at ~500 nm, which is similar to wild-type enzyme. The formation of charge-transfer complex (CTC) exhibits a strong peak at 540 nm and profoundly influences the absorbance spectra of TXNRD1, leading to the absence of the shoulder at ~500 nm [31,32]. This phenotype indicated that the guiding bar mutant did not result in a spontaneous formation of charge-transfer complex between Cys^{64} and FAD in the absence of NADPH.

We subsequently examined the capacity of TXNRD1 variants to form charge-transfer complexes when NADPH was introduced into the system. Evidently, the formation of the charge-transfer complex was increased in the Y402F, W407F, and N418A/N419A mutants compared to the wild-type TXNRD1, while F406A mutant exhibited a lower potential (Fig. 1G and Fig. S5).

Considering the potential differences in charge-transfer complex formation, we conducted a thorough analysis of the TXNRD1 variants using Excitation-Emission Matrix (EEM) fluorescence spectrum analysis [33,34], which may provide additional insights into the mechanisms and properties of TXNRD1. Typical enzyme-bound flavin fluorescence at Em_{max} ~520 nm has three excitation peaks at Ex_{max} ≈280 nm, ≈370 nm, and ≈470 nm [34]. We detected three excitation peaks of Ex_{max} at 320 nm, 380 nm, and 430 nm for the wild-type TXNRD1 at Em_{max} ~520 nm (Fig. 1H). Conversely, the Y402F mutation resulted in the loss of the Ex_{max} peaks at 430 nm, while the F405A, F406A and N418A/N419A mutations of TXNRD1 exhibited a new peak at approximately 390–400 nm. Y402A, W407F, W407A, W411F and W411A mutants presented similar excitation peaks compared to the wild-type enzyme (Fig. S6). These results demonstrated the communication between the guiding bar and its neighboring aromatic residues with the FAD co-factor, and

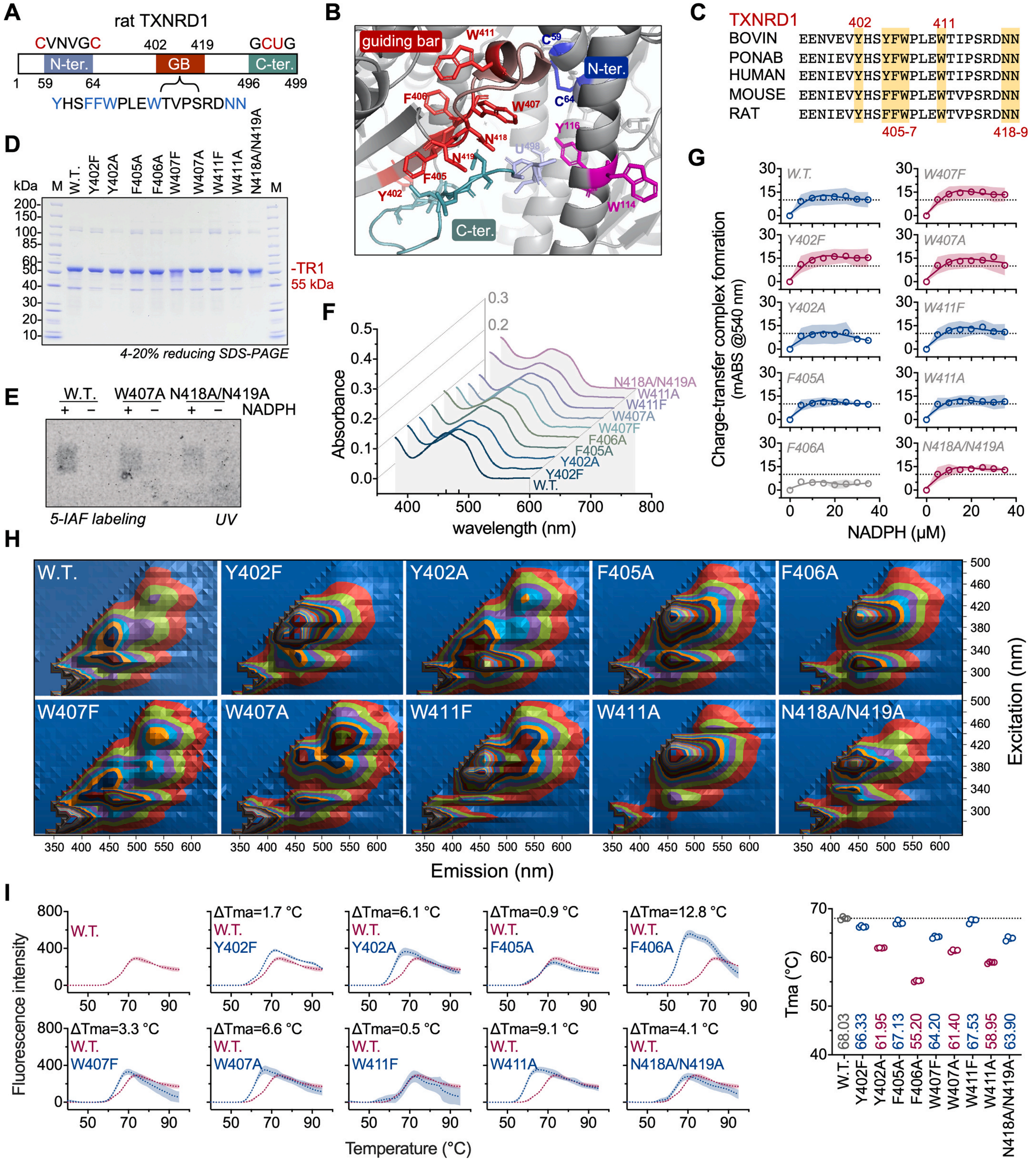

Fig. 1. The guiding bar motif of TXNRD1 interacts with the co-factor FAD. **(A)** Schematic diagram for the catalytic motifs of TXNRD1. GB, guiding bar motif. **(B)** Structure of the guiding bar motif in rat TXNRD1. The conformation was obtained from PDB: 3EAN. **(C)** Partial sequence alignment of the guiding bar motif of mammalian TXNRD1. The aromatic amino acid residues were highlighted in yellow. **(D)** SDS-PAGE analysis of TXNRD1 variants. **(E)** 5-IAF labelling of TXNRD1 and its two mutant variants, W407A and N418A/N419A. **(F)** Wavelength scanning analysis. The UV–Vis spectra of TXNRD1 and its variants (7 μM) were scanned in a range from 300 nm to 700 nm. **(G)** Formation of charge-transfer complexes in mutant variants of rat TXNRD1. The charge-transfer complex of TXNRD1 was determined at 540 nm in the presence of NADPH at indicated concentrations. **(H)** Excitation-Emission Matrix fluorescence spectra of TXNRD1 mutant variants. 7 μM of TXNRD1 variants were loaded into a flat-bottomed 96-well black plate for 3-D fluorescence measurements. **(I)** Differential Scanning Fluorimetry analysis of TXNRD1 and its mutant variants. The Tma values are showed in the right panel.

mutations in these residues have a profound impact on the electron flow of the enzyme.

2.4. Mutation of the aromatic amino acid in guiding bar motif affects the thermostability of TXNRD1

We then examined the thermostability of TXNRD1 variants using Differential Scanning Fluorimetry (DSF) analysis [35,36]. The wild-type TXNRD1 exhibited a Tma of 68.03 °C (Fig. 1I). Remarkably, mutations of Y402A, F406A, W407A and W411A strongly decreased the thermostability of TXNRD1 (ΔTma >5 °C). Additionally, N418A/N419A exhibited a ΔTma of 4.1 °C. These data strongly suggest that the guiding bar also acts as a stabilizer for TXNRD1. We speculated that the phenotype is attributed to the aromatic side chain of these residues. Mutating tyrosine (Y402) or tryptophan (W407, W411) residues to alanine (Y402A, W407A, and W411A) had a more pronounced impact on thermostability than mutating them to phenylalanine (Y402F, W407F, and W411F) (Fig. 1I). Collectively, these results revealed that the guiding bar motif is critical for ensuring the thermostability of TXNRD1.

2.5. Guiding bar is vital for the disulfide bond reduction activity of TXNRD1

TXNRD1 has a broad substrate spectrum and several well-characterized substrates, including TXN, TRP14, DTNB, 9,10-PQ, toxoflavin, and juglone [9,22,37,38]. In this experiment, we aimed to determine the kinetic parameters of TXNRD1 and its variants when mutating the guiding bar. The activity of TXNRD1 is highly dependent on Sec^{498}, which is encoded by the UGA stop codon. Although several methods have been proposed [39–43], it remains still challenging to produce high-quality selenoproteins due to unwanted premature termination of protein synthesis and misincorporation at the position of selenocysteine [44,45]. To address the incorporation ratio of selenocysteine, we utilized ICP-MS to determine the selenium content of each TXNRD1 variant. The selenium content of wild-type TXNRD1 is 35 %, accompanied by a specific activity of 26.8 U/mg in the DTNB reduction assay. The selenium contents of TXNRD1 variants range from 16 % to 26 % (Fig. 2A). Kinetic parameters were subsequently determined and normalized based on the respective selenium contents as indicated.

In the reduction of disulfide bond using substrates such as TXN1, TRP14, and DTNB, most variants exhibited a slight decrease in catalytic efficiency compared with wild-type TXNRD1. Specifically, in TXN1 reduction, mutants such as Y402A, W407F and W407A increased the k_{cat} values but lowered the enzyme's affinity for TXN, resulting in decreased catalytic efficiency (approximately 50 % for Y402A, 90 % for W407F, and 80 % for W407A). In contrast to wild-type TXNRD1, the K_m values of TXNRD1 variants are essentially unchanged in both DTNB reduction and cystine-coupled TRP14 reduction. However, k_{cat} numbers were lower, resulting in much lower k_{cat}/K_m values (Fig. 2B). Simultaneously, we observed a notable reduction in the efficiency of F406A in reducing three substrates by approximately 3–4 fold. Meanwhile the N418A/N419A is the only TXNRD1 variant that increases the TRP14 reduction, aligning with its capacity to form a CTC (Fig. 1G). Collectively, mutations in the guiding bar motif of TXNRD1 resulted in a modest decrease in catalytic efficiency of TXNRD1's disulfide reductase activity. This decrease can be attributed to a lower affinity for the substrates and a reduced turnover rate in response to the substrates.

2.6. Guiding bar motif hinders Sec-independent reduction of juglone on TXNRD1

The reduction of toxoflavin and 9,10-PQ by TXNRD1 has been previously reported to be selenium-dependent [9,37]. In this study, we observed that the U498C variant of TXNRD1 exhibited a comparatively lower activity to reduce 9,10-PQ and toxoflavin (Fig. 2C and D), indicating that these two substrates may not strictly depend on selenium for their reduction by TXNRD1. Nevertheless, wild-type TXNRD1 displayed significantly higher turnover numbers in reducing these substrates compared to Sec-deficient variants (Fig. 2D). Therefore, the turnover numbers for the reduction of 9,10-PQ and toxoflavin were also adjusted based on the selenium contents.

Remarkably, the catalytic efficiency (k_{cat}/K_m) in both toxoflavin and 9,10-PQ reduction notably increased in W407F, W407A and N418A/N419A mutants of TXNRD1 (Fig. 2B). Intriguingly, the turnover numbers of certain mutants in toxoflavin reduction either remained unchanged or decreased. For instance, the k_{cat} value for both Y402A and W411A is approximately 85 % of the wild-type enzyme, while the K_m values are roughly 3.5-fold lower than the W.T., resulting in an increase in their catalytic efficiency. This phenomenon was also observed in the 9,10-PQ reduction, where the K_m values of the mutant variants were generally 2-3-fold lower than those of the wild-type enzyme (Fig. 2B).

Interestingly, we found a noticeable increase in the catalytic activity of the guiding bar mutant of TXNRD1 for juglone reduction (Fig. 2B). The activity of juglone reduction was affected by W407F, the k_{cat} increased for approximately 3-fold whereas K_m was decreased for ~1.3-fold, thereby resulting in an efficiency of ~ 4-fold higher than the wild-type TXNRD1. As previously demonstrated, the reduction of juglone by TXNRD1 is supported in a Sec-independent manner and is believed to primarily occur through the N-terminal -CVNVGC-/FAD motif [22,46]. These results demonstrate that the TXNRD1 variants with the guiding bar mutations are all functional in terms of NADPH usage and FAD binding, and exhibit increased catalytic efficiency in terms of Sec-independent reduction.

It has been proposed that the guiding bar residues prevent electron leakage from the N-terminal redox center [12]. This offers plausible explanation for the increase in catalytic efficiency in Sec-independent reduction (like juglone reduction) instead of the disulfide bond (such as the Cys^{32}-Cys^{35} of TXN) reduction in guiding bar mutated TXNRD1. The mutations appear to facilitate greater accessibility of substrates, particularly small molecules, to the N-terminus, allowing them to undergo reduction by the N-terminal -CVNVGC-/FAD motif. This is evidenced by the Cys^{59} and Cys^{64} mutants still exhibiting reduced activity in juglone reduction (Fig. 2E).

Furthermore, the heightened Sec-independent activity of TXNRD1 with guiding bar residue mutations was also observed in other characterized Sec-independent substrates previously reported [47–49], such as plumbagin and menadione (Fig. 2F). These collective findings strongly support the conclusion that the guiding bar motif restricts the Se-independent reduction activity of TXNRD1.

2.7. Guiding bar motif protects the Sec-containing C-terminal tail from electrophilic reagents like TRi-1

In the catalytic process of TXNRD1, Sec^{498} acts as the attacking residue for the TXN1-disulfide (Cys^{32} and Cys^{35}). Consequently, the solvent-exposed Sec^{498} residue can be easily conjugated by electrophiles [50,51]. Given the electron flows within the enzyme may be affected the guiding bar, our subsequent objective was to examine the impact of the guiding bar motif on inhibitor binding. We selected TRi-1 [21,52], RSL3 [53,54], auranofin [55], and cisplatin [56] as inhibitors of TXNRD1 in this scenario. Surprisingly, mutation of the guiding bar residues increased the inhibition rate of TRi-1 on TXNRD1 (Fig. 3A). After incubating with 0.5 μM TRi-1 for 15 min, the wild-type TXNRD1 retained approximately 30 % activity, whereas the TXNRD1 variants almost completely lost their activity (the residual activity <10 %). The inhibition of RSL3 on TXNRD1 showed a similar pattern to TRi-1, indicating that the guiding bar motif prevents the selenocysteine from reacting with electrophilic reagents. However, the inhibition of auranofin and cisplatin on TXNRD1 is not significantly affected by guiding bar mutants (Fig. 3A), confirming the preventive effect of guiding bar on TXNRD1 is focused on the selenocysteine-containing tail.

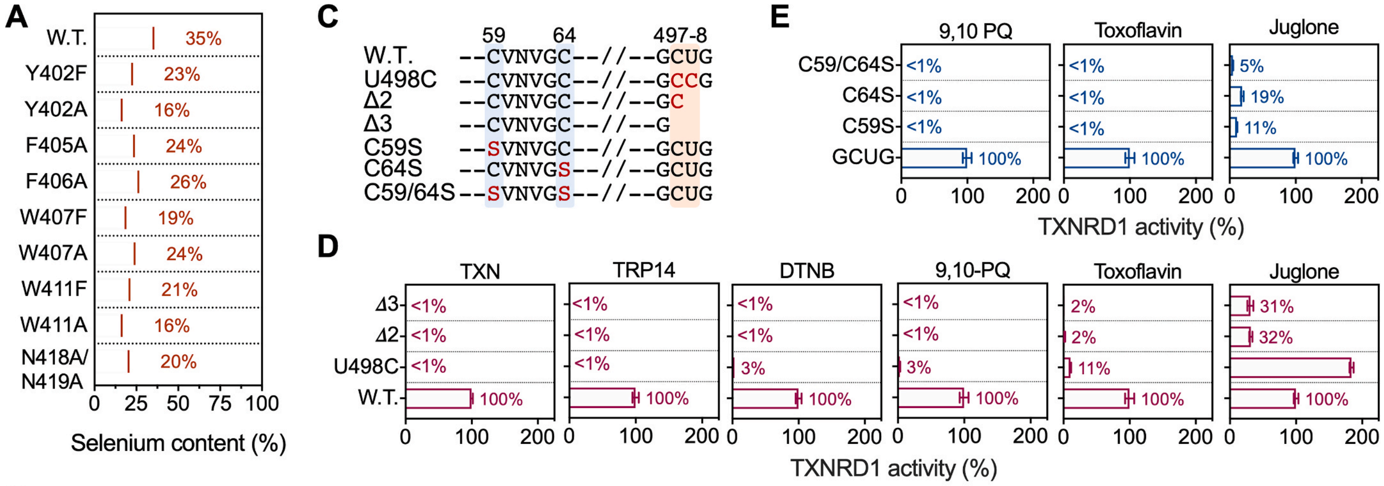

B

TXNRD1 Variants	W.T.	Y402F	Y402A	F405A	F406A	W407F	W407A	W411F	W411A	N418A/N419A
DTNB[a]										
k_{cat}(min^{-1})	3902.3	4109.2	2531.7	2870.4	1405.8	2991.9	2553.0	3060.6	2421.7	3355.7
K_m(μM)	70.8	54.3	44	109	78.9	124.6	93.7	123	85.4	87.9
k_{cat}/K_m(μM min^{-1})	55.1	75.7	57.5	26.3	17.8	24.0	27.2	24.9	28.4	38.2
TXN (Insulin)[a]										
k_{cat}(min^{-1})	3189.5	4533.9	3331.2	3096.8	6414.7	3886.9	4395.1	4050.5	5492.5	5986.9
K_m(μM)	9.9	13.4	20	13.8	70.6	12.7	15.9	9.7	23.9	22.9
k_{cat}/K_m(μM min^{-1})	322.2	338.3	166.6	224.4	90.9	306.1	276.4	417.6	229.8	261.4
TRP14 (Cystine)[a]										
k_{cat}(min^{-1})	3717.7	4227.3	2839.5	3032.9	2006.6	3187.5	3420.9	3725.7	3240.1	4355.3
K_m(μM)	2.3	2.9	3.8	3.1	4.1	2.7	3.1	2.6	3.2	2.6
k_{cat}/K_m(μM min^{-1})	1616.4	1457.7	747.2	978.4	489.4	1180.6	1103.5	1432.9	1012.5	1675.1
9,10-PQ[a]										
k_{cat}(min^{-1})	4916.2	3433.6	2404.2	2652.9	2101.7	3118.1	3549.9	3882.9	3435.6	3635.7
K_m(μM)	4.3	1.9	3.2	2	1.8	1.7	1.8	2.3	2	1.4
k_{cat}/K_m(μM min^{-1})	1143.3	1807.2	751.3	1326.5	1167.6	1834.2	1972.1	1688.2	1717.8	2596.9
Toxoflavin[a]										
k_{cat}(min^{-1})	1537.4	2766.7	1205.0	1866.1	1396.7	1387.0	1623.1	1840.4	1342.3	1524.4
K_m(μM)	17.8	13.5	5.5	4.9	15.57	5.7	4	4.2	3.1	3.9
k_{cat}/K_m(μM min^{-1})	86.4	204.9	219.1	380.8	89.7	243.3	405.8	438.2	433.0	390.9
Juglone										
k_{cat}(min^{-1})	426.7	675.7	400.0	1447	568.9	1233	1904	594.2	618.3	877.2
K_m(μM)	6.0	5.2	3.1	7.8	3.2	4.5	8.0	5.0	7.6	5.3
k_{cat}/K_m(μM min^{-1})	71.1	129.9	129.0	185.5	177.8	274.0	238.0	118.8	81.4	165.5

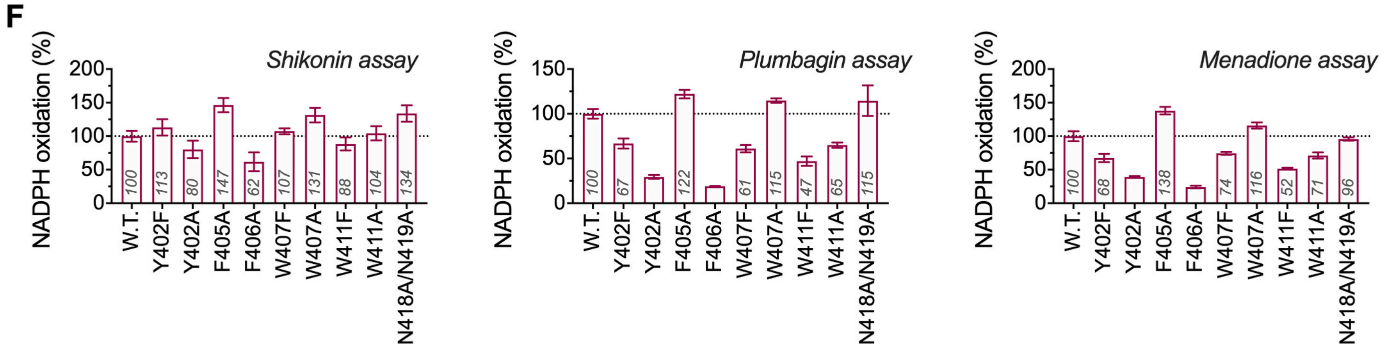

Fig. 2. Mutating the guiding bar motif increases the Sec-independent activity of TXNRD1. (A) Determination of selenium contents of TXNRD1 variants using ICP-MS. The selenium contents of TXNRD1 and its mutant variants (0.2 mg/mL) were determined by ICP-MS. **(B)** Kinetic parameters of TXNRD1 variants using different substrates. a, The activity was normalized based on the Se content. **(C)** Schematic diagram of the C-terminal and N-terminal TXNRD1 mutants used in this study. The redox active cysteine and selenocysteine were labeled. **(D)** Sec-dependent and -independent reductions of TXNRD1. **(E)** Relative activity of TXNRD1 with mutations at the N-terminal redox motif. **(F)** Relative NADPH oxidation activity of TXNRD1 and its variants. 100 μM Shikonin, plumbagin and menadione were used as the substrates of TXNRD1 (30 nM) in the presence of 200 μM NADPH.

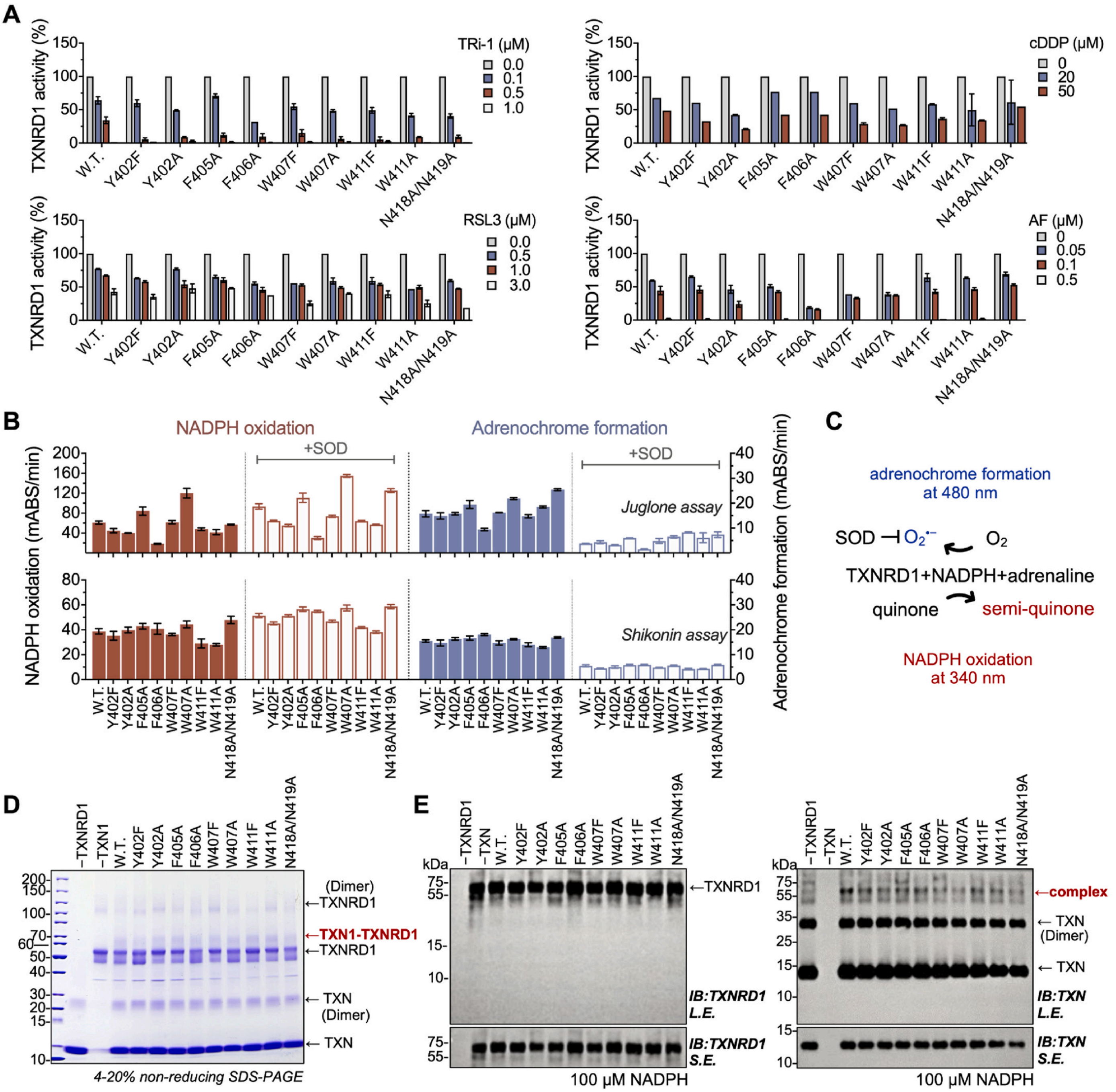

Fig. 3. Guiding bar motif of TXNRD1 protects the Sec-containing C-terminal tail from attacks of electrophilic reagents. **(A)** Inhibitory effect of electrophilic reagents on TXNRD1. NADPH-reduced TXNRD1 (0.2 μM) was incubated separately with TRi-1, RSL3 and auranofin for 15 min, or with cisplatin for 60 min. The residual activity of TXNRD1 was determined by using DTNB reducing assay. **(B)** Quantitative analysis of SecTRAPs. The reaction mixtures contained 50 nM TXNRD1 and its variants, 200 μM NADPH, 1 mM epinephrine and either 10 μM juglone or 100 μM shikonin in TE buffer with or without 10 units/well SOD as indicated. Changes in absorbance were measured simultaneously at both 340 nm and 480 nm. **(C)** Mechanism for the superoxide ions detection. **(D)** Formation of the TXNRD1-TXN1 complex induced by cisplatin. 1 μM of TXNRD1 or its variants were incubated with 8 μM TXN1 and 100 μM cisplatin at room temperature for 16 h. The samples were then analyzed by non-reducing SDS-PAGE followed by CBB stain. **(E)** Formation of the TXNRD1-TXN1 complex induced by NADPH. 1 μM of TXNRD1 or its variants were incubated with 8 μM TXN1 and 200 μM NADPH at room temperature for 16 h. The samples were then analysis by a non-reducing Western blot. L.E., long exposure; S.E., short exposure.

Given the guiding bar motif of TXNRD1 in modulating electron flow and electrophile modification, we were intrigued to explore its association with inhibitor binding and the formation of SecTRAPs. SecTRAPs are known to be formed from TXNRD1 after electrophilic targeting at its Sec residue or removing the catalytic residue at the C-terminus of TXNRD1 [20]. Numerous intensive studies have revealed that SecTRAPs are devoid of TXN reductase activity but retain the inherent NADPH oxidation activity, resulting in the production of superoxide anion and hydrogen peroxide [46,57]. We demonstrated that the mutation at the guiding bar motif retained the superoxide anion production activity of TXNRD1 from SecTRAPs. The addition of superoxide dismutase (SOD) suppressed the oxidation of adrenaline to adrenochrome by superoxide anions (Fig. 3B and C). Furthermore, W407A and N418A/N419A mutants increase the production of superoxide anions (Fig. 3B). These results are consistent with the increased Sec-independent reduction activity of TXNRD1 variants when the guiding bar was mutated.

2.8. *TXNRD1 variants with guiding bar mutation continue to form complexes with TXN1*

Numerous studies have shown that cisplatin forms a complex with TXN1 and TXNRD1, known as TXN1-TXNRD1 (TTR) complex [56], which can also be initiated by NADPH [34]. A non-reducing SDS-PAGE analysis revealed that the mutations in the guiding bar did not have profound effects on the TXN1-TXNRD1 complex induced by cisplatin (Fig. 3D and Fig. S7). Subsequently, we verified the formation of the TXN1-TXNRD1 complex induced by NADPH. Unfortunately, no noticeable TXN1-TXNRD1 complex was observed in non-reducing SDS-PAGE using CBB stain (Fig. S8). So, we performed non-reducing Western blotting to detect the formation of TXN1-TXNRD1 complexes (Fig. 3E and Fig. S9). The guiding bar mutants of TXNRD1 exhibited the ability to form complexes with TXN1 in the presence of NADPH. This is consistent with the result obtained from 5-IAF labeling that the guiding bar mutant of the enzyme could be reduced by NADPH through the reductive half-reaction and further reduce its substrates. These results suggest that mutations in the guiding bar motif of TXNRD1 still lead to the formation of a stable complex with TXN1 in the presence of NADPH or cisplatin.

2.9. *Inhibiting TXNRD1 activity by CSD peptide*

In addition to its role in the catalysis process of TXNRD1, we noticed that the guiding bar motif is also pre-defined as a caveolin binding motif (CBM, amino acids 402–411). This motif is characterized by its high content of aromatic amino acids and interacts with the scaffolding protein caveolin-1. Previously, Volonte and Galbiati first reported the inhibition of TXNRD1 by caveolin-1 [58]. The scaffolding domain of caveolin-1 (amino acids 82–101) directly binds to the CBM of TXNRD1 [58]. However, it is still argued whether the caveolin scaffolding domain (CSD) interacts with the CBM motif of proteins, as this motif is normally buried internally [59].

Here, we investigated the interaction between CSD and TXNRD1 using a synthesized peptide (Fig. 4A). CAV-X was a peptide commonly used as a negative control for the CSD-derived peptide [60–63]. The peptide is hydrophobic and is dissolved in DMSO. We initially verified the stability of the peptide in the water-based buffer system. After being incubated in TE buffer for 1 h, no significant changes were observed in the turbidity and absorption peak of 20 μM CSD peptide (Fig. 4B). We then determined whether the CSD could accept the electrons from TXNRD1. When compared with plumbagin, a substrate of TXNRD1 [48], we found that the CSD peptide is not a proper substrate for TXNRD1 (Fig. 4C). However, the CSD peptide inhibited the DTNB reducing activity of TXNRD1, as well as the juglone and 9,10-PQ reduction activity (Fig. 4D). The inhibition of CSD on the TXN reductase activity of

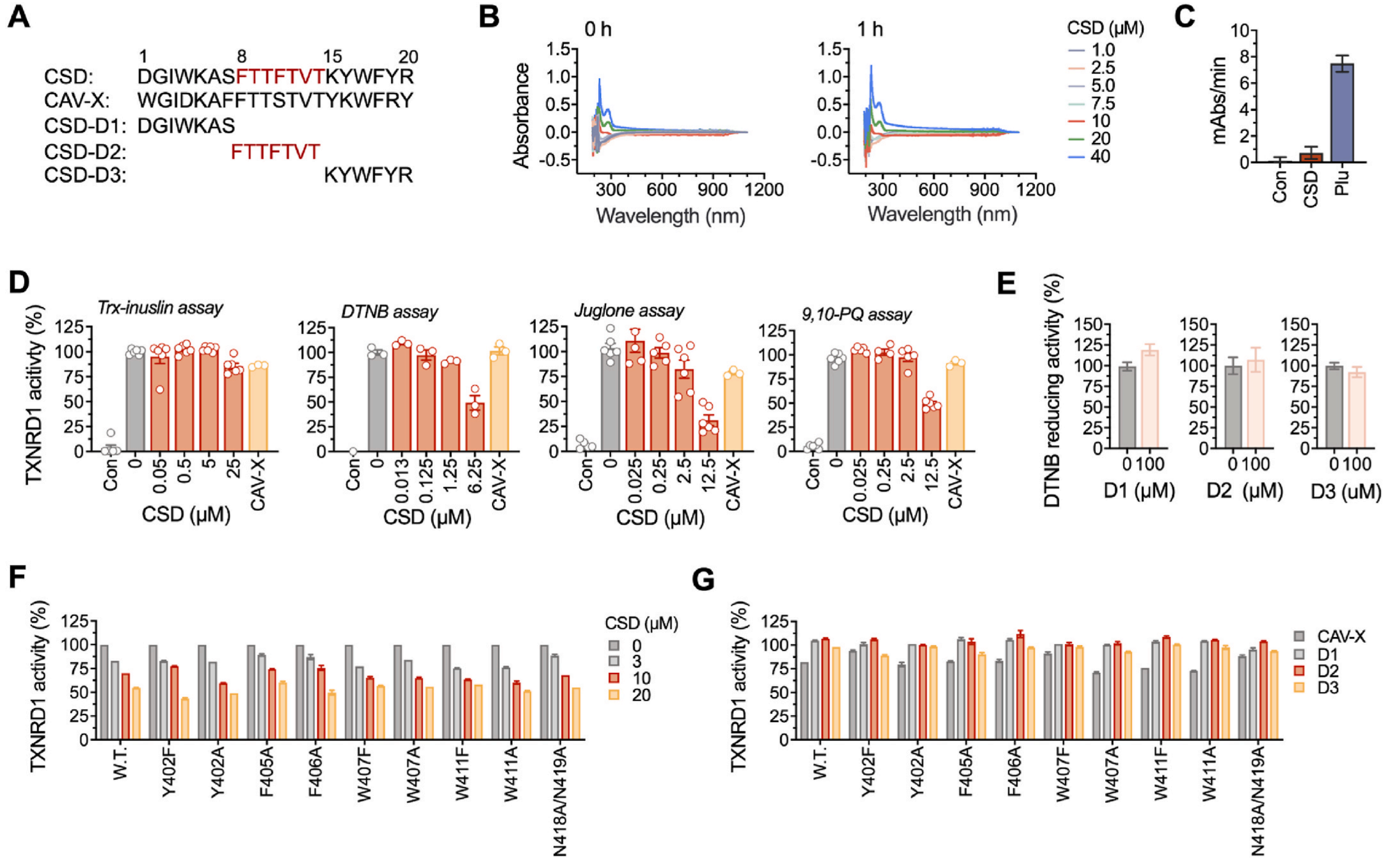

Fig. 4. Caveolin-1 scaffolding domain (CSD) peptide inhibits TXNRD1 activity. (A) Sequences of CSD, CAV-X, CSD-D1, CSD-D2, and CSD-D3 peptides. **(B)** Stability analysis of CSD peptides through wavelength scanning. The CSD peptide was diluted in TE buffer with concentrations ranging from 0 to 40 μM. The spectrum of CSD peptide was assayed at 0 min and 60 min, respectively. **(C)** Electron transfer activity of TXNRD1 upon CSD peptide. The reaction mixture contained 30 nM TXNRD1, 200 μM NADPH, 10 μM CSD peptide, or 30 μM plumbagin. The NADPH oxidation was measured to determine the potential electron transfer from TXNRD1 to the CSD peptide or plumbagin. **(D)** Inhibition of CSD peptide on TXNRD1. The effects of CSD peptide on TXNRD1-mediated reduction were assayed using TXN1, DTNB, juglone and 9,10-PQ as substrates. The activity of TXNRD1 was measured using the standard method, with the addition of indicated concentrations of CSD peptide. **(E)** Effects of truncated CSD peptides (D1/D2/D3) on the activity of TXNRD1. The effects of CSD-D1, D2, and D3 peptides on TXNRD1 activity were determined using DTNB reduction assay. **(F–G)** Analysis of CSD-derived peptides on TXNRD1 activity. The DTNB reducing activity of TXNRD1 variants in the presence of CSD peptide (0–20 μM) and CSD-derived peptides (20 μM) was assayed.

TXNRD1 is similar to that of control peptide CAV-X (Fig. 4D). These results demonstrated that CSD peptide inhibits the activity of recombinant TXNRD1 *in vitro*.

We next wanted to further investigate the inhibition details of the CSD peptide on TXNRD1. Generally, the inhibitors of TXNRD1 harbor electrophilic properties and target the Sec residue of TXNRD1. To clarify the inhibition mechanism, we employed a desalting column to eliminate the CSD-peptide from the incubation system. This method is commonly utilized to detect the irreversible inhibition of TXNRD1 [21,22]. However, we did not detect any TXNRD1 activity in the elution fractions (Fig. S10), which was also observed in the affinity chromatography using either His-tagged TXNRD1 or His-tagged CSD peptide (Fig. S10). Unfortunately, we are currently unable to verify the inhibition mechanism of the CSD peptide on TXNRD1. However, we have demonstrated that this inhibition exhibits a slightly time-dependent character (Fig. S11).

The FTTFTVT is considered the core domain of the CSD peptide [62]. We showed that neither domain 1 of CSD (CSD-D1), nor domains 2 and 3 (CSD-D2 and CSD-D3) (Fig. 4A) exhibited any inhibitory effect on TXNRD1 (Fig. 4E), indicating that the complete sequence of the CSD-peptide is important for the inhibition of TXNRD1. Furthermore, using the guiding bar mutant of TXNRD1, we demonstrated that the inhibition of CSD derived peptide on TXNRD1 is not affected by the single amino acid mutant of TXNRD1 (Fig. 4F and G). Taken together, these results indicated that the CSD peptide inhibits TXNRD1 activity *in vitro*, but not by binding to the CBM of TXNRD1.

2.10. LCS3 inhibits recombinant TXNRD1 in a reversible manner via the nitro group

Recently, Lockwood and colleagues demonstrated the selective growth impairment of human lung adenocarcinoma (LUAD) cells by a compound named LCS3, attributed to its inhibition of cellular TXNRD1 [64]. We herein investigated the potential effect of LCS3 on TXNRD1 by using recombinantly expressed mutants of the enzyme (Fig. 5A). Clearly, LCS3 exhibited strong inhibition of the physiological TXN reductase activity on the recombinant TXNRD1 (Fig. 5B). The IC_{50} value of LCS3 for the TXN reductase activity is 10.7 μM. However, compared with the TXN reductase activity, the inhibition of LCS3 on the TRP14 reductase activity of TXNRD1 is relatively low. 20 μM LCS3 in the reaction mixture still retained over 90 % of the activity of the TRP14-coupled cystine reduction of TXNRD1 (Fig. 5B). Meanwhile, LCS3 exhibited an inhibitory effect on the GSR, with an IC_{50} value of 28.6 μM (Fig. 5C), which is consistent with previously reported findings [64]. The reversible inhibition was also confirmed to be non-time-dependent (Fig. 5D). To further confirm the reversible inhibition, we removed the free LCS3 by using a desalting column. The enzyme activity was significantly rescued compared with the intact enzyme (Fig. 5E), indicating that LCS3 is a reversible inhibitor of TXNRD1.

When testing the inhibition of LCS3 on TXNRD1 with various substrates, we observed that the inhibition of LCS3 on TXNRD1 was substrate-specific. Specifically, some substrates, such as juglone and toxoflavin, were not strongly inhibited by LCS3 (Fig. 5F). The DTNB reduction of TXNRD1 is potently inhibited by LCS3, with an IC_{50} value of 42.1 μM. Meanwhile, a LCS3 analogue, compound without a nitro group (LCS3-ΔN), did not inhibit TXNRD1 and GSR, suggesting that the nitro group in LCS3 is the functional group responsible for the inhibitory effect (Fig. G). In cellular circumstances, after incubating HCT116 cells with LCS3 for 4 h, the TXNRDs activity and protein level in the extracted cell lysate were not altered. This also confirmed that LCS3 does not function as an irreversible inhibitor of TXNRD1 (Fig. 5H). Together, these results indicated that LCS3 inhibits the TXN reductase activity of purified TXNRD1 reversibly *in vitro.*

2.11. LCS3 efficiently inhibits TXNRD1 activity but is not through the interaction with the guiding bar

The interaction between LCS3 and TXNRD1 is predicted by *in silico* simulation, as previously reported. To elucidate the potential interacting residue of LCS3 on TXNRD1, we utilized mutant variants of TXNRD1 and conducted the inhibition of LCS3 on the enzyme and its variants. The activity loss of Sec-deficient TXNRD1, inhibited by LCS3, is weaker compared to the Sec-containing enzyme in DTNB reduction (Fig. 5I). It should also be noted that the DTNB reduction activity of the Sec-deficient TXNRD1 mutant is approximately 1–5% of the wild-type enzyme, but it is still detectable, as demonstrated in Fig. 2D.

We further investigated the inhibition effect of LCS3 on the guiding bar mutant of TXNRD1. Surprisingly, we did not observe a significant change in the dose-response curve of the inhibition effect on TXRND1 mutant variants by LCS3 (Fig. 5J). The W411A and W411F mutants retained approximately 65 % activity of the untreated enzyme, which is highly similar to the wild-type TXNRD1 (Fig. 5J). Area Under Curve (AUC) analysis revealed no difference among TXNRD1 mutant variants in the inhibition by LCS3 (Fig. 5K).

Additionally, TXNRD1 can be classified into a high-MW form, which is a selenoprotein that primarily exists in higher organisms, and a low-MW form, which could be found in prokaryotic organisms. The low-MW form is not a selenoprotein and lacks a guiding bar motif [1]. Interestingly, we demonstrated that LCS3 exhibited a potent inhibitory effect on the recombinant TrxR of *Acinetobacter baumannii* and *Klebsiella pneumoniae,* with IC_{50} values of 1.81 μM and 12.4 μM for ACIBA and KLEPN TrxR, respectively (Fig. 5L).

We then recombinantly produced TXNRD1 variants at D82, R416, and D417 (Fig. 5M), which are predicted to be the binding residues of LCS3 on TXNRD1 using *in silico* simulation. We first determined the activity of these mutant variants. Notably, these three mutants showed a strongly decrease in TXN reduction, and the activity of DTNB reduction is impaired (Fig. 5N and Fig. S12). We then investigated the inhibition of LCS3 on TXNRD1 variants. Similar to the wild-type enzyme, these three mutants exhibited the same inhibition pattern by LCS3 (Fig. 5O).

Collectively, these findings strongly suggest that the inhibition of LCS3 on thioredoxin reductases is not dependent on the guiding bar motif.

3. Discussion

Selenoprotein TXNRD1 has been widely investigated, however, the guiding bar motif in relation to both the catalytic mechanism and redox regulation of TXNRD1 has remained to be an extensive attention [12]. Distinct from flavoproteins such as dihydrolipoyl dehydrogenase (DLD) and GSR, TXNRD1 contains a unique flexible Sec-containing C-terminal tail, which has a significant impact on the catalytic activity [31,65,66]. The guiding bar motif is positioned parallel to the C-terminal tails in the opposite direction of the catalytic pocket, suggesting that guiding bar motif does not directly contribute to the enzyme's electron transfer [11,12]. Nevertheless, mutations in the residues of guiding bar motif were observed to affect the formation of the charge-transfer complex (CTC) of the enzyme. Although the CTC is monitored in the EH_4-formed enzyme using a UV–Vis spectrophotometer instead of a stopped-flow spectrometer [67], the results still demonstrated the electron transfer capacity in the absence of the substrates. As shown in Fig. 1F, Y402F, W407F and N418A/N419A significantly increased the absorbance at 540 nm at high concentrations of NADPH. In contrast, the formation of CTC for F406A was quite low. These results were consistent with the EEM data and kinetic parameters, showing that the F406A mutant significantly decreased the catalytic efficiency. Meanwhile, the EEM data demonstrated that the mutation affects the enzyme's binding to FAD. Previous studies have revealed that Trp^{114} residue interacts with FAD, and that the fluorescence spectra of FAD are altered by the mutant form of Trp^{114}, rather than by alterations in the C-terminal residues [34]. Given the

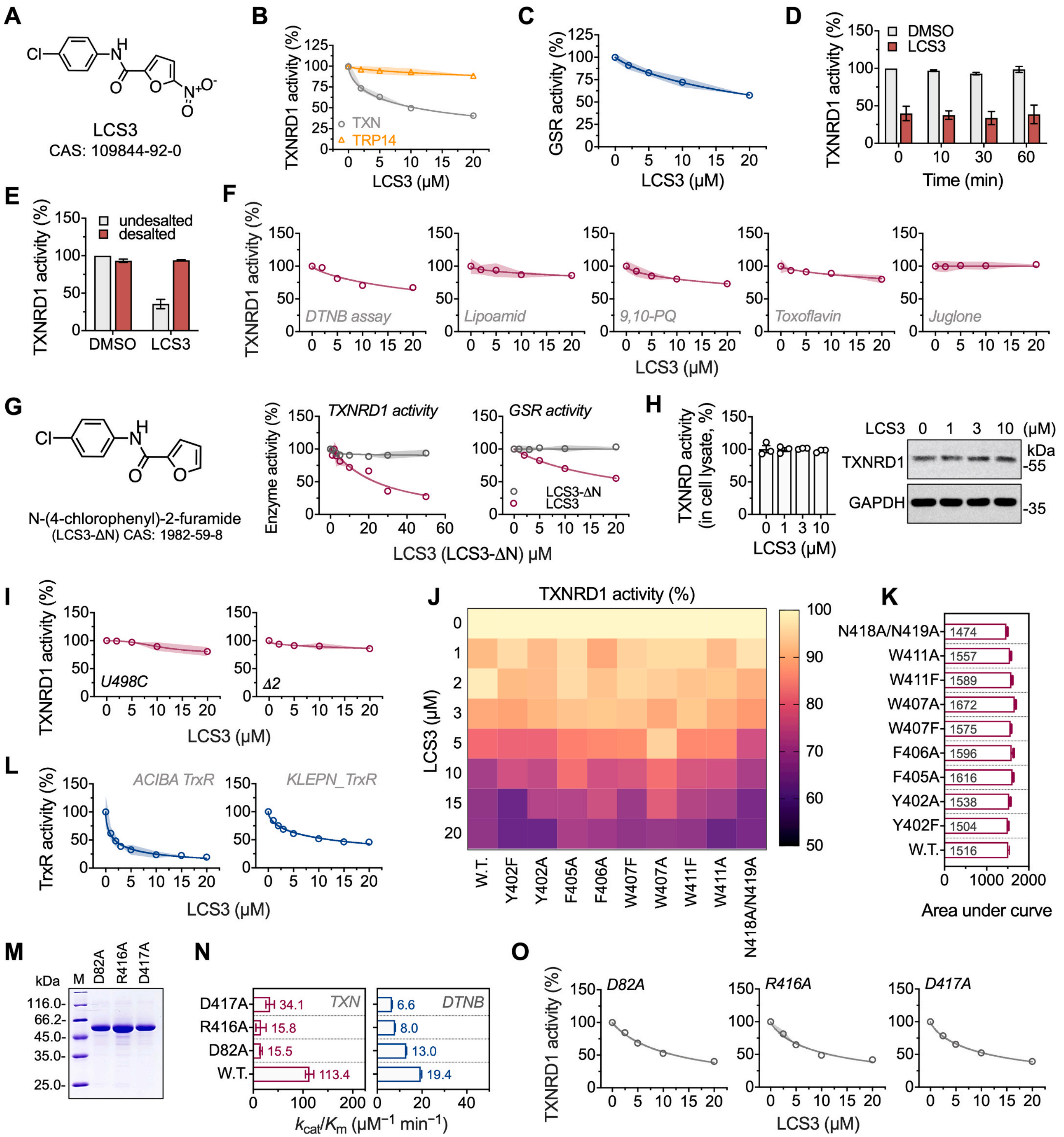

Fig. 5. LCS3 is a non-covalent inhibitor of TXNRD1 particularly inhibiting its TXN1 reductase activity. (A) Chemical structure of LCS3. **(B)** Inhibition of the TXN1 reductase activity of TXNRD1 by LCS3. The reaction mixture contained 50 nM TXNRD1, 10 μM TXN, 200 μM NADPH, 160 μM insulin, and various concentrations of LCS3. **(C)** LCS3 inhibits the GSSG reduction activity of GSR. The reaction mixture contained 2 nM GSR, 1 mM GSSG, and various concentrations of LCS3. **(D)** The time-course inhibition of LCS3 on TXNRD1. 50 μM LCS3 was incubated with 20 nM TXNRD1 for the indicated time. The final LCS3 concentration is 25 μM. The activity of TXNRD1 was measured using the DTNB reducing assay. **(E)** Restored TXNRD1 after removing the LCS3 through desalting. 20 nM TXNRD1 was incubated with 50 μM LCS3 and a NAP-5 desalting column was used for removing the free LCS3 from the incubation system. **(F)** Effect of LCS3 on the reducing activity of TXNRD1 independent of disulfide exchange. TXNRD1 activity in the presence of LCS3 was assayed by measuring the reduction of 9,10-PQ, juglone, and toxoflavin. **(G)** Inhibition of TXNRD1 and GSR activity by LCS3 analogue LCS3-ΔN. TXNRD1 activity was determined by DTNB reducing and GSR activity was assayed by GSSG reduction. **(H)** TXNRDs activity and protein levels in the cell lysate of HCT116 cells treated with LCS3. HCT116 cells were treated with various concentrations of LCS3 for 4 h. **(I)** Inhibition of Sec-deficient TXNRD1 by LCS3. **(J, K)** Inhibition of the TXNRD1 with guiding bar residue mutation by LCS3. The activities of TXNRD1 and its variants were determined by DTNB reducing assay. The values of area under curve are shown in (J). **(L)** Inhibition of low-weight thioredoxin reductase by LCS3. **(M)** SDS-PAGE analysis of D82A, R416A, and D417A mutants of TXNRD1. **(N)** Kinetic analysis of D82A, R416A, and D417A mutants of TXNRD1. **(O)** Inhibition of D82A, R416A, and D417A mutants of TXNRD1 by LCS3.

Trp^{114} and guiding bar residues are far away from the FAD based in the TXNRD1 structure, this change may be explained by the transformation of the interaction between the N-terminal domain and FAD.

Furthermore, our data strongly suggested that the guiding bar motif affects the kinetic parameters by modulating the movement of the C-terminal tail. In this study, we performed the site-directed mutagenesis at the residues located at the guiding bar motif and found such mutations significantly increase the Sec-independent reduction but decrease the disulfide reductase activity of the enzyme. We proposed that the increase is a consequence of enhanced substrate accessibility to the FAD/-CVNVGC- domain, as the increase in catalytic efficiency is primarily attributed to the lower K_m values. Additionally, it could also be inferred that the mutation may affect the nucleophilic attack of Cys^{59} on the selenenylsulfide between Sec^{498} and Cys^{497} [2,5].

Moreover, mutations in the guiding bar motif affect the binding of inhibitors to the enzyme. In the experiments, we selected TRi-1, RSL3, auranofin, and cisplatin to test their inhibitory effect on TXNRD1. TRi-1 stands out as one of the most specific inhibitors of TXNRD1, targeting the Sec^{498} residues with lower GSH binding activity [21,52]. RSL3 is a well-known ferroptosis inducer, by inhibiting GPX4 through modification of the selenocysteine or cysteine residues [53,54]. TXNRD1 has recently been identified as the cellular target of RSL3 [36]. Additionally, auranofin and cisplatin are widely accepted FDA-approved drugs that inhibit cellular TXNRD1 activity, but they do not specifically target selenocysteine [55,68]. Our data revealed that the mutated enzyme is more susceptible to attack by TRi-1 and RSL3. This can be explained by the rearranging effect of the guiding bar on the Sec-containing C-terminal tail of the enzyme, making the selenocysteine more accessible to the drug. These results suggested an important role of the guiding bar motif as a gatekeeper for the reactive C-terminal tail.

Caveolae are a characteristic feature of the plasma membrane (PM) in many mammalian cell types, and caveolin-1 is the major protein that composes caveolae [69]. It has been demonstrated that numerous proteins utilize the conserved caveolin-binding motif (CBM) to interact with caveolae via the caveolin scaffolding domain (CSD). TXNRD1 has been reported to interact with caveolin-1 through the amino acid region 402–411, which coincides with the guiding bar motif of the enzyme [58]. However, there is still an argument on the CBM/CSD-dependent interactions in caveolar signaling since CBM is generally buried and not readily accessible in most proteins [59,70]. Therefore, we would investigate the interaction of CSD peptides on the guiding bar. Clearly, the synthesized CSD peptides inhibited the activity of TXNRD1 *in vitro* compared to the control peptide CAV-X (Fig. 4D). CSD-D2 (CSP7) was considered the central domain of the CSD both *in vitro* and *in vivo* [62,63]. However, when using truncated peptides, we observed that the truncated peptides do not inhibit TXNRD1 activity, indicating that the inhibitory effect of CSD on the enzyme is highly dependent on the structural integrity of CSD (Fig. 4A–E). Additionally, by using CBM mutant of the enzyme, we observed that the inhibition of CSD peptide is not dependent on the CBM residue, which supports the opinion that the CBM/CSD-dependent interactions are unlikely to mediate caveolar signaling. Interestingly, it has been discovered that caveolae can sense oxidative stress by regulating the NRF2 antioxidant response [71]. Additionally, a rare v3 splice form of TXNRD1 was found to potentially target the membrane [72]. However, it is not yet clear if these findings are related to the interaction between TXNRD1 and caveolin-1, and the precise role of this interaction in cellular signaling remains to be fully understood. Further studies are needed to elucidate the details of this interaction.

Numerous studies have revealed that TXNRD1 is upregulated in cancer cells [73,74]. In cancer treatment, pharmacological inhibition of TXNRD1 induces rapid cell death through SecTRAPs [20,75], while TXNRD1 deficiency renders cells susceptible to glutathione (GSH) depletion [76,77]. These findings position TXNRD1 as a promising and compelling drug target for cancer therapy. Recently, a small molecule lung cancer screen 3 (LCS3) was developed to suppress the growth of LUAD. Thermal proteomic profiling (TPP) identified TXNRD1 as the cellular target of LCS3 [64,78]. Additionally, *in silico* molecular docking predicted that the nitro group of LCS3 forms a hydrogen bond with Trp^{411} of TXNRD1. LCS3 is also predicted to interact with Asp^{82} through hydrogen bond formation, and with Arg^{416} through an arene-cation interaction [64]. Given that the docking analysis predicts that the LCS3 interacts with residues in guiding bar located homodimer interfaces of TXNRD1, we investigated the inhibition details of LCS3 on TXNRD1. It is surprising that LCS3 is a reversible inhibitor of TXNRD1, which differs from most inhibitors of TXNRD1 (Fig. 5B–E). Right now, many inhibitors of TXNRD1 are electrophilic and modifying the enzyme through alkylation of thiols or selenols [23,51,79–81]. Using recombinant protein, we identified that the nitro group of LCS3 profoundly inhibits the enzyme (Fig. 5G). However, when we determined the residue target of LCS3 on TXNRD1 by using mutant variants of the enzyme, we observed that the W411, as well as D82, R416 and D417, mutants of TXNRD1 did not impact the inhibitory effect (Fig. 5J, K, O). In addition, the inhibition of LCS3 on low-MW TrxR1 is more potent than high-MW form, suggesting that LCS3 may not interact with the guiding bar. However, these findings also offer a potential application as an antibacterial agent through the inhibition of TrxR. Taken together, it is impressive to find LCS3 as a reversible inhibitor of TXNRD1, and further clarification is needed regarding the inhibition mechanism and the structure-function relationship.

In conclusion, the results obtained in this study provide valuable insights into the catalytic mechanism of TXNRD1 and demonstrate that the distinctive guiding bar motif functions as a gearbox for tuning the flexible C-terminal tail and adjusting the catalytic activity of TXNRD1.

4. Materials and methods

4.1. Chemicals and reagents

Chemicals used in this study include: 5-Hydroxy-1,4-naphthoquinone (juglone, H47003, Sigma-Aldrich), N-(4-chlorophenyl)-2-furamide (L134759, Sigma-Aldrich), 5,5′-dithiobis-(2-nitrobenzoic acid) (DTNB, S19139, Yuanye), nicotinamide adenine dinucleotide phosphate (NADPH, S10103, Yuanye), TRi-1 (S87818, Yuanye), auranofin (S80655, Yuanye), Shikonin (B21682, Yuanye), LCS3 (S89617, Yuanye), 9,10-phenanthrene quinone (9,10-PQ, P106382, Aladdin), RSL3 (R302648, Aladdin), HED (B152479, Aladdin), L-cystine (BD21525, Bidepharm), cisplatin (MB1055-2, MeilunBio), yeast extract (LP0021B, Oxoid), tryptone (LP0042B, Oxoid).

Antibodies used in this study include: TXNRD1 (67728, Proteintech), TXN (66475, Proteintech), goat anti-mouse IgG (SA00001-1, Proteintech).

Critical commercial assays used in this study include: BCA protein kit (P0012, Beyotime), Bradford protein kit (20202ES76, Yeasen, China), 4–20 % SDS-PAGE gel (P0469M, Beyotime; M00657, Gensrcipt).

Proteins used in this study include: SOD (S7571, Sigma-Aldrich), BSA (NA8692, Ruibio), Insulin (S12033, Yuanye). Recombinant TXN [38], GSR [8], TRP14 [38], *Acinetobacter baumannii* (ACIBA) TrxR [82] and *klebsiella pneumoniae* (KLEPN) TrxR [82] were produced as previous described.

4.2. Strains and constructs

The *E. coli* BL21 (DE3) *gor*$^-$ host strain was generously provided by Prof. Arne Holmgren (Karolinska Institutet, Stockholm, Sweden). Plasmids pSUABC and pET-TRS_{TER} were gifts from Prof. Elias S.J. Arnér (Karolinska Institutet, Stockholm, Sweden). Primers for constructing the TXNRD1 mutants in guiding bar motif were listed in Table S1.

4.3. Generation and purification of recombinant rat TXNRD1

Recombinant rat TXNRD1 and its mutant variants were produced as described unless otherwise stated [30,83]. In brief, the pET-TR-S_{TER}-derived plasmids are co-transformed into BL21 (DE3) *gor*⁻ with plasmid pSUABC (D82A, R416A and D417A mutants of TXNRD1 were produced in BL21 (DE3) strain). The bacterial cell cultures were incubated in a shaker (220 rpm) at 37 °C until $OD_{600nm} = 2.4$ reaching late points of the log phase. Then 0.5 mM IPTG, 5 μM selenite, and 100 μg/mL L-cysteine were separately added into the bacterial cultures. The cultures were continually incubated at 24 °C for 24 h in the shaker, bacterial cells were harvested by centrifugation at 3500 rpm for 20 min, and the wet bacterial pellets were subsequently resuspended in lysis buffer (50 mM Tris-HCl, 20 mM EDTA, 1 mg/mL lysozyme, pH = 7.4), followed with freeze-thawing for 3 cycles and the viscous nucleic acids were broken by sonication on ice. Lysates were spun down at 12,000 rpm, 4 °C for 30 min. Afterwards, the supernatant was purified through affinity chromatography on 2′5′ ADP Sepharose 4B (17070001, Cytiva, Sweden), and size-exclusion chromatography on HiPrep 16/60 Sephacryl S-300 HR (17116701, Cytiva, Sweden). Recombinant proteins were analyzed by reducing SDS-PAGE and stained by Coomassie Brilliant Blue (CBB).

4.4. 5-IAF labeling of TXNRD1

3 μM TXNRD1 and its variants (pH 8.5) in oxidized states were separately incubated with 1 mM 5-iodoacetamidofluorescein (5-IAF) for 30 min in the dark at room temperature. In parallel, 3 μM enzymes were pre-reduced with 1 mM NADPH for 15 min, followed by the addition of 1 mM 5-IAF and incubation in dark for 30 min at room temperature. All 5-IAF-labeled protein samples were then desalted and subjected to a reducing SDS-PAGE gel, visualized under the UV light.

4.5. Wavelength scanning of various TXNRD1 mutants

Wavelength scanning (340 nm–600 nm) was determined by using a spectrophotometer (UV5-Bio, Mettler Toledo, Switzerland). 6.5 μM TXNRD1 and its mutants were separately added into a standard 1-cm quartz cuvette to analyze the spectrum with TE buffer as reference.

4.6. Charge-transfer complex detection

Charge-transfer complex detection of TXNRD1 and its variants were performed in a microplate reader (SpectraMax ABS, Molecular Devices). The abs at 540 nm of 6.5 μM wild-type TXNRD1 and its variants in the presence of indicated concentrations of NADPH were determined. The enzyme lacking NADPH was regarded as the reference.

4.7. Excitation-emission matrix spectroscopy

Wild-type TXNRD1 and its variants (7 μM) were dissolved in TE buffer (pH 7.5). 100 μL of enzymes were loaded into a flat-bottomed 96-wells black plate for fluorescence measurements using a multimode reader (Synergy H1, Bio-Tek, USA). The emission spectrum ranging from 300 nm–700 nm was obtained by exiting the sample at a fixed excitation wavelength of 260 nm and subsequently the excitation wavelength was increased by 10-nm intervals up to 510 nm with TE buffer as reference. The data obtained for all excitation wavelengths were used to plot the fluorescence emission spectra in 3D format, with ‘X-axis’ as the excitation wavelength (Ex), ‘Y-axis’ as the emission wavelength (Em), and the ‘Z-axis’ as fluorescence intensity.

4.8. Kinetic analyses of TXNRD1 variants

Enzymatic activities of purified TXNRD1 variants were determined in transparent 96-well microtiter plates using classical substrates including DTNB, juglone, 9,10-PQ, toxoflavin, human TXN1, and human TRP14 as described [84,85]. The standard reaction mixture contained 10–100 nM TXNRD1 or its mutant variants, 200–300 μM NADPH in TE buffer. All the activity assays were performed at room temperature either following TNB^- formation at 412 nm ($\varepsilon_{TNB-} = 13{,}600\ M^{-1}\ cm^{-1}$) for DTNB, or directly following NADPH consumption as decrease at 340 nm ($\varepsilon_{NADPH} = 6200\ M^{-1}\ cm^{-1}$) for the other substrates. Insulin and cystine were used as the electron acceptor for TXN1 reduction and TRP14 reduction, respectively. Activity measurements were performed in triplicate (unless stated in the text) using a microplate reader (SpectraMax ABS, Molecular Devices). Kinetic constants were calculated with the Prism 8 software (GraphPad) after direct plotting of the velocity versus substrate concentration followed by automatic Michaelis–Menten fit with nonlinear regression.

4.9. Quantification of superoxide anions production

In vitro superoxide production was assayed according to the adrenochrome method [48]. The standard reaction mixture (200 μl) contains 200 μM NADPH, 1 mM epinephrine, 50 nM TXNRD1, and 10 μM juglone or 100 μM shikonin as indicated. Changes in absorbance at 340 nm and 480 nm were measured simultaneously, using the same reaction mixture without the enzyme as the reference. For validation of superoxide being formed, superoxide dismutase (SOD) was added (10 units/well). All reactions were performed in a microplate reader (SpectraMax ABS, Molecular Devices, USA).

4.10. Synthesis of CSD-derived peptides

The CSD peptide and its derived peptides were synthesized by Sangon Biotech (Shanghai, China) as sequences follows: CSD (DGIWKASFTTFTVTKYWFYR), CAV-X (WGIDKAFFTTSTVTYKWFRY), CSD-D1 (DGIWKAS), CSD-D2 (FTTFTVT), and CSD-D3 (KYWFYR). The peptides were freshly dissolved in DMSO up to 4 mM before experiments.

4.11. Cell culture and LCS3 treatment

HCT116 cells (CL-0096, Procell) were cultured in McCoy’s 5A medium supplemented with 10 % fetal bovine serum (FBS, 164210, Procell), 100 U/mL penicillin, 100 mg/mL streptomycin (P/S, AC03L332, Life-iLab) in a humidified incubator (Heal Force) with an atmosphere of 5 % CO_2 and a temperature of 37 °C. As for the LCS3 treatment, in brief, HCT116 cells were seeded into 6-well plates at 400,000 cells per well and treated with LCS3 for 4 h. The cells were washed with PBS buffer three times and all adherent cells were lysed by the RIPA buffer with 1 mM protease inhibitor PMSF. Then, the cell extract was centrifuged at 18,000 *g* at 4 °C for 20 min. Total protein contents were determined using a BCA kit (Beyotime, China).

4.12. Cellular TXNRD1 activity

Cellular TXNRDs activities were determined according to TXN1-coupled end-point insulin assay as previously established [28,86] and the method was slightly modified in this experiment. In brief, an appropriate amount of cell lysates was added into a master mixture containing 80 mM Hepes buffer (pH 7.5), 15 μM TXN1, 300 μM insulin, 660 μM NADPH, and 3 mM EDTA. A reaction mixture without TXN1 was used as a background control. Samples were incubated at 37 °C for 30 min. Subsequently, 6.0 M guanidine hydrochloride containing 1 mM DTNB, and 20 mM EDTA was added to each well, and an endpoint Abs @412 nm was measured and recorded. TXNRDs activities of cell lysates were normalized to protein concentrations for an accurate comparison.

4.13. Western blotting

The total protein concentrations of cell lysates were determined through BCA protein assay. All samples were incubated at 95 °C for 10 min before SDS–PAGE analysis and then transferred onto the PVDF membrane (0.45 μm, Millipore). The membranes were blocked by 5 %

skimmed milk for 1 h and incubated with indicated concentrations of primary antibody overnight at 4 °C: TXNRD1 (1: 5000), TXN (1: 5000). After washed with TBST three times, the blots were incubated with the secondary antibody (1: 5000) for 1 h at room temperature. The ECL mixture solution (ED0015/ED0016, Sparkjade, Shandong, China) was added to the membranes and developed by imaging analyzer (Sage-creation, Beijing).

4.14. Analysis of the TXN1-TXNRD1 complexes

TXN1 was initially reduced with 10 mM DTT at 37 °C for 20 min, followed by removal of the DTT using a NAP-5™ desalting column. Wild-type TXNRD1 or its variants (1 μM) were incubated with 8 μM TXN1, along with 200 μM NADPH or 100 μM cisplatin as indicated at room temperature for 16 h. All samples were mixed with 5 × SDS loading solution without (non-reducing) or with (reducing) addition of 20 mM DTT and denatured at 95 °C for 10 min. Then, the samples were loaded onto an SDS-PAGE gel and followed with CBB stain or Western blotting.

4.15. GSR activity assay

Glutathione reductase (GSR) activity was determined using the oxidized glutathione (GSSG) as a substrate [8]. The standard assay system (200 μL) contains 1 mM GSSG, 2 nM yeast GSR, and 200 μM NADPH in TE buffer, pH7.5. GSR activity was calculated by following the NADPH oxidation based on the absorbance decrease at 340 nm ($\varepsilon_{\text{NADPH}} = 6200\ \text{M}^{-1}\ \text{cm}^{-1}$). The assays were repeated for three times and mean value was used to calculate the GSR activity.

4.16. Differential Scanning Fluorimetry (DSF) assay

The DSF analysis was performed as described [35]. Briefly, TXNRD1 and its variants were diluted in a DSF buffer (20 mM HEPES, pH 7.4, 100 mM NaCl) to 3 μM. Then, a SYPRO Orange stain (S5506, Thermo Fisher) was added with a final concentration of 5 × . The fluorescence signal was acquired using the CG-05 fluorescence spectrometer (Heal Force, China) with an excitation wavelength of 498 nm and fluorescence emission at 522 nm. The temperature was raised from 35 to 95 °C with a ramp rate of 1 °C/min. Three biological replicates were conducted for each condition, and their means and standard deviations are shown.

4.17. Statistical analysis

The data were presented as the Mean ± SD (n = 3). Statistical differences between the two groups were analyzed using the Student's t-test. Comparisons among multiple groups were statistically assessed by one-way analysis of variance (ANOVA) and followed by a post hoc Scheffe test. The significant differences between groups were defined as $* p < 0.05$, $**p < 0.01$, and $***p < 0.001$, where n.s. means not significant.

Funding

This research was funded by National Natural Science Foundation of China (U22A20455 & 31670767), Fundamental Research Funds for the Central Universities (DUT17JC36, DUT20LK36 and DUT21LK29).

CRediT authorship contribution statement

Wuyang Shi: Investigation, Visualization. **Shibo Sun:** Conceptualization, Investigation, Visualization, Writing – original draft, Writing – review & editing. **Haowen Liu:** Investigation, Visualization. **Yao Meng:** Investigation. **Kangshuai Ren:** Investigation. **Guoying Wang:** Investigation. **Minghui Liu:** Investigation. **Jiaqi Wu:** Investigation. **Yue Zhang:** Investigation. **Huang Huang:** Investigation. **Meiyun Shi:** Resources. **Weiping Xu:** Funding acquisition, Resources. **Qiang Ma:** Resources. **Bingbing Sun:** Funding acquisition, Resources. **Jianqiang Xu:** Conceptualization, Funding acquisition, Supervision, Writing – original draft, Writing – review & editing.

Declaration of competing interest

The authors declare that they have no known competing financial interests or personal relationships that could have appeared to influence the work reported in this paper.

Data availability

Data will be made available on request.

Acknowledgments

The authors want to thank Prof. Dr. Elias S.J. Arnér (Karolinska Institutet, Sweden) for his material supports, Prof. Dr. Enyin Lai (Zhejiang University, China) for his experimental assistances, and Prof. Dr. Jianing Zhang (Dalian University of Technology, China) for his scientific discussion.

Appendix A. Supplementary data

Supplementary data to this article can be found online at https://doi.org/10.1016/j.redox.2024.103050.

References

[1] J. Lu, A. Holmgren, The thioredoxin antioxidant system, Free Radic. Biol. Med. 66 (2014) 75–87.
[2] E.S.J. Arnér, Focus on mammalian thioredoxin reductases–important selenoproteins with versatile functions, Biochim. Biophys. Acta 1790 (6) (2009) 495–526.
[3] M. Dagnell, E.E. Schmidt, E.S.J. Arnér, The A to Z of modulated cell patterning by mammalian thioredoxin reductases, Free Radic. Biol. Med. 115 (2018) 484–496.
[4] L. Zhong, E.S. Arner, A. Holmgren, Structure and mechanism of mammalian thioredoxin reductase: the active site is a redox-active selenolthiol/selenenylsulfide formed from the conserved cysteine-selenocysteine sequence, Proc. Natl. Acad. Sci. U. S. A. 97 (11) (2000) 5854–5859.
[5] Q. Cheng, T. Sandalova, Y. Lindqvist, E.S.J. Arnér, Crystal structure and catalysis of the selenoprotein thioredoxin reductase 1, J. Biol. Chem. 284 (6) (2009) 3998–4008.
[6] W. Brandt, L.A. Wessjohann, The functional role of selenocysteine (Sec) in the catalysis mechanism of large thioredoxin reductases: proposition of a swapping catalytic triad including a Sec-His-Glu state, Chembiochem 6 (2) (2005) 386–394.
[7] A. Andor, M. Mohanraj, Z.A. Pato, K. Uri, B. Biri-Kovacs, Q. Cheng, et al., TXNL1 has dual functions as a redox active thioredoxin-like protein as well as an ATP- and redox-independent chaperone, Redox Biol. 67 (2023) 102897.
[8] J. Xu, E.S. Arner, Pyrroloquinoline quinone modulates the kinetic parameters of the mammalian selenoprotein thioredoxin reductase 1 and is an inhibitor of glutathione reductase, Biochem. Pharmacol. 83 (6) (2012) 815–820.
[9] R. Gencheva, Q. Cheng, E.S.J. Arnér, Efficient selenocysteine-dependent reduction of toxoflavin by mammalian thioredoxin reductase, Biochim. Biophys. Acta Gen. Subj. (2018).
[10] L. Xia, T. Nordman, J.M. Olsson, A. Damdimopoulos, L. Bjorkhem-Bergman, I. Nalvarte, et al., The mammalian cytosolic selenoenzyme thioredoxin reductase reduces ubiquinone. A novel mechanism for defense against oxidative stress, J. Biol. Chem. 278 (4) (2003) 2141–2146.
[11] K. Fritz-Wolf, S. Urig, K. Becker, The structure of human thioredoxin reductase 1 provides insights into C-terminal rearrangements during catalysis, J. Mol. Biol. 370 (1) (2007) 116–127.
[12] K. Fritz-Wolf, S. Kehr, M. Stumpf, S. Rahlfs, K. Becker, Crystal structure of the human thioredoxin reductase-thioredoxin complex, Nat. Commun. 2 (2011) 383.
[13] A.P. Lothrop, G.W. Snider, E.L. Ruggles, R.J. Hondal, Why is mammalian thioredoxin reductase 1 so dependent upon the use of selenium? Biochemistry 53 (3) (2014) 554–565.
[14] A.P. Lothrop, G.W. Snider, E.L. Ruggles, A.S. Patel, W.J. Lees, R.J. Hondal, Selenium as an electron acceptor during the catalytic mechanism of thioredoxin reductase, Biochemistry 53 (4) (2014) 654–663.
[15] E.S.J. Arnér, Selenoproteins-What unique properties can arise with selenocysteine in place of cysteine? Exp. Cell Res. 316 (8) (2010) 1296–1303.
[16] D.L. Hatfield, P.A. Tsuji, B.A. Carlson, V.N. Gladyshev, Selenium and selenocysteine: roles in cancer, health, and development, Trends Biochem. Sci. 39 (3) (2014) 112–120.

[17] H.J. Reich, R.J. Hondal, Why nature chose selenium, ACS Chem. Biol. 11 (4) (2016) 821–841.

[18] J.P. O'Keefe, C.M. Dustin, D. Barber, G.W. Snider, R.J. Hondal, A "seleno effect" differentiates the roles of redox active cysteine residues in plasmodium falciparum thioredoxin reductase, Biochemistry 57 (11) (2018) 1767–1778.

[19] A.P. Lothrop, G.W. Snider, S. Flemer Jr., E.L. Ruggles, R.S. Davidson, A.L. Lamb, et al., Compensating for the absence of selenocysteine in high-molecular weight thioredoxin reductases: the electrophilic activation hypothesis, Biochemistry 53 (4) (2014) 664–674.

[20] K. Anestal, S. Prast-Nielsen, N. Cenas, E.S. Arner, Cell death by SecTRAPs: thioredoxin reductase as a prooxidant killer of cells, PLoS One 3 (4) (2008) e1846.

[21] W.C. Stafford, X. Peng, M.H. Olofsson, X. Zhang, D.K. Luci, L. Lu, et al., Irreversible inhibition of cytosolic thioredoxin reductase 1 as a mechanistic basis for anticancer therapy, Sci. Transl. Med. 10 (428) (2018).

[22] J. Xu, Q. Cheng, E.S. Arner, Details in the catalytic mechanism of mammalian thioredoxin reductase 1 revealed using point mutations and juglone-coupled enzyme activities, Free Radic. Biol. Med. 94 (2016) 110–120.

[23] Y. Zhang, S. Sun, W. Xu, R. Yang, Y. Yang, J. Guo, et al., Thioredoxin reductase 1 inhibitor shikonin promotes cell necroptosis via SecTRAPs generation and oxygen-coupled redox cycling, Free Radic. Biol. Med. 180 (2022) 52–62.

[24] O. Rackham, A.M. Shearwood, R. Thyer, E. McNamara, S.M. Davies, B.A. Callus, et al., Substrate and inhibitor specificities differ between human cytosolic and mitochondrial thioredoxin reductases: implications for development of specific inhibitors, Free Radic. Biol. Med. 50 (6) (2011) 689–699.

[25] S.K. Burley, G.A. Petsko, Aromatic-aromatic interaction: a mechanism of protein structure stabilization, Science 229 (4708) (1985) 23–28.

[26] C. Shih, A.K. Museth, M. Abrahamsson, A.M. Blanco-Rodriguez, A.J. Di Bilio, J. Sudhamsu, et al., Tryptophan-accelerated electron flow through proteins, Science 320 (5884) (2008) 1760–1762.

[27] M.T. Zhang, L. Hammarstrom, Proton-coupled electron transfer from tryptophan: a concerted mechanism with water as proton acceptor, J. Am. Chem. Soc. 133 (23) (2011) 8806–8809.

[28] R. Yang, S. Sun, Y. Guo, Y. Meng, H. Liu, M. Shi, et al., Anti-inflammatory effect of dimethyl fumarate associates with the inhibition of thioredoxin reductase 1 in RAW 264.7 cells, Molecules 28 (1) (2022) 107.

[29] E.S.J. Arnér, H. Sarioglu, F. Lottspeich, A. Holmgren, A. Bock, High-level expression in Escherichia coli of selenocysteine-containing rat thioredoxin reductase utilizing gene fusions with engineered bacterial-type SECIS elements and co-expression with the selA, selB and selC genes, J. Mol. Biol. 292 (5) (1999) 1003–1016.

[30] J. Xu, V. Croitoru, D. Rutishauser, Q. Cheng, E.S. Arner, Wobble decoding by the Escherichia coli selenocysteine insertion machinery, Nucleic Acids Res. 41 (21) (2013) 9800–9811.

[31] L.D. Arscott, S. Gromer, R.H. Schirmer, K. Becker, C.H. Williams Jr., The mechanism of thioredoxin reductase from human placenta is similar to the mechanisms of lipoamide dehydrogenase and glutathione reductase and is distinct from the mechanism of thioredoxin reductase from Escherichia coli, Proc. Natl. Acad. Sci. U. S. A. 94 (8) (1997) 3621–3626.

[32] L. Johansson, L.D. Arscott, D.P. Ballou, C.H. Williams Jr., E.S. Arner, Studies of an active site mutant of the selenoprotein thioredoxin reductase: the Ser-Cys-Cys-Ser motif of the insect orthologue is not sufficient to replace the Cys-Sec dyad in the mammalian enzyme, Free Radic. Biol. Med. 41 (4) (2006) 649–656.

[33] A.W. Munro, M.A. Noble, Fluorescence analysis of flavoproteins, Methods Mol. Biol. 131 (1999) 25–48.

[34] J. Xu, S.E. Eriksson, M. Cebula, T. Sandalova, E. Hedstrom, I. Pader, et al., The conserved Trp114 residue of thioredoxin reductase 1 has a redox sensor-like function triggering oligomerization and crosslinking upon oxidative stress related to cell death, Cell Death Dis. 6 (2015) e1616.

[35] T. Wu, M. Hornsby, L. Zhu, J.C. Yu, K.M. Shokat, J.E. Gestwicki, Protocol for performing and optimizing differential scanning fluorimetry experiments, STAR Protoc 4 (4) (2023) 102688.

[36] D.M. Cheff, C. Huang, K.C. Scholzen, R. Gencheva, M.H. Ronzetti, Q. Cheng, et al., The ferroptosis inducing compounds RSL3 and ML162 are not direct inhibitors of GPX4 but of TXNRD1, Redox Biol. 62 (2023) 102703.

[37] N. Cenas, H. Nivinskas, Z. Anusevicius, J. Sarlauskas, F. Lederer, E.S.J. Arnér, Interactions of quinones with thioredoxin reductase: a challenge to the antioxidant role of the mammalian selenoprotein, J. Biol. Chem. 279 (4) (2004) 2583–2592.

[38] I. Pader, R. Sengupta, M. Cebula, J. Xu, J.O. Lundberg, A. Holmgren, et al., Thioredoxin-related protein of 14 kDa is an efficient L-cystine reductase and S-denitrosylase, Proc. Natl. Acad. Sci. U. S. A. 111 (19) (2014) 6964–6969.

[39] C. Aldag, M.J. Brocker, M.J. Hohn, L. Prat, G. Hammond, A. Plummer, et al., Rewiring translation for elongation factor Tu-dependent selenocysteine incorporation, Angew Chem. Int. Ed. Engl. 52 (5) (2013) 1441–1445.

[40] Q. Cheng, E.S. Arnér, Selenocysteine insertion at a predefined UAG codon in a release factor 1 (RF1)-depleted Escherichia coli host strain bypasses species barriers in recombinant selenoprotein translation, J. Biol. Chem. 292 (13) (2017) 5476–5487.

[41] J.K. Eaton, L. Furst, R.A. Ruberto, D. Moosmayer, A. Hilpmann, M.J. Ryan, et al., Selective covalent targeting of GPX4 using masked nitrile-oxide electrophiles, Nat. Chem. Biol. 16 (5) (2020) 497–506.

[42] Z. Fan, J. Song, T. Guan, X. Lv, J. Wei, Efficient expression of glutathione peroxidase with chimeric tRNA in amber-less Escherichia coli, ACS Synth. Biol. 7 (1) (2018) 249–257.

[43] B. Eckenroth, K. Harris, A.A. Turanov, V.N. Gladyshev, R.T. Raines, R.J. Hondal, Semisynthesis and characterization of mammalian thioredoxin reductase, Biochemistry 45 (16) (2006) 5158–5170.

[44] X. Fu, D. Soll, A. Sevostyanova, Challenges of site-specific selenocysteine incorporation into proteins by Escherichia coli, RNA Biol. 15 (4–5) (2018) 461–470.

[45] T. Hilal, B.Y. Killam, M. Grozdanovic, M. Dobosz-Bartoszek, J. Loerke, J. Burger, et al., Structure of the mammalian ribosome as it decodes the selenocysteine UGA codon, Science 376 (6599) (2022) 1338–1343.

[46] Q. Cheng, W.E. Antholine, J.M. Myers, B. Kalyanaraman, E.S.J. Arnér, C.R. Myers, The selenium-independent inherent pro-oxidant NADPH oxidase activity of mammalian thioredoxin reductase and its selenium-dependent direct peroxidase activities, J. Biol. Chem. 285 (28) (2010) 21708–21723.

[47] S. Sun, W. Xu, Y. Zhang, Y. Yang, Q. Ma, J. Xu, Menadione inhibits thioredoxin reductase 1 via arylation at the Sec(498) residue and enhances both NADPH oxidation and superoxide production in Sec(498) to Cys(498) substitution, Free Radic. Biol. Med. 172 (2021) 482–489.

[48] S. Sun, Y. Zhang, W. Xu, R. Yang, Y. Yang, J. Guo, et al., Plumbagin reduction by thioredoxin reductase 1 possesses synergy effects with GLUT1 inhibitor on KEAP1-mutant NSCLC cells, Biomed. Pharmacother. 146 (2022) 112546.

[49] J. Li, X. Zuo, P. Cheng, X. Ren, S. Sun, J. Xu, et al., The production of reactive oxygen species enhanced with the reduction of menadione by active thioredoxin reductase, Metallomics 11 (9) (2019) 1490–1497.

[50] F. Saccoccia, F. Angelucci, G. Boumis, D. Carotti, G. Desiato, A.E. Miele, et al., Thioredoxin reductase and its inhibitors, Curr. Protein Pept. Sci. 15 (6) (2014) 621–646.

[51] J. Zhang, D. Duan, Z.L. Song, T. Liu, Y. Hou, J. Fang, Small molecules regulating reactive oxygen species homeostasis for cancer therapy, Med. Res. Rev. 41 (1) (2021) 342–394.

[52] P. Sabatier, C.M. Beusch, R. Gencheva, Q. Cheng, R.A. Zubarev, E.S.J. Arnér, Comprehensive chemical proteomics analyses reveal that the new TRi-1 and TRi-2 compounds are more specific thioredoxin reductase 1 inhibitors than auranofin, Redox Biol. 48 (2021) 102184.

[53] S.J. Dixon, K.M. Lemberg, M.R. Lamprecht, R. Skouta, E.M. Zaitsev, C.E. Gleason, et al., Ferroptosis: an iron-dependent form of nonapoptotic cell death, Cell 149 (5) (2012) 1060–1072.

[54] H. Liu, F. Forouhar, A.J. Lin, Q. Wang, V. Polychronidou, R.K. Soni, et al., Small-molecule allosteric inhibitors of GPX4, Cell Chem. Biol. 29 (12) (2022) 1680–16893, e9.

[55] C. Marzano, V. Gandin, A. Folda, G. Scutari, A. Bindoli, M.P. Rigobello, Inhibition of thioredoxin reductase by auranofin induces apoptosis in cisplatin-resistant human ovarian cancer cells, Free Radic. Biol. Med. 42 (6) (2007) 872–881.

[56] S. Prast-Nielsen, M. Cebula, I. Pader, E.S.J. Arnér, Noble metal targeting of thioredoxin reductase–covalent complexes with thioredoxin and thioredoxin-related protein of 14 kDa triggered by cisplatin, Free Radic. Biol. Med. 49 (11) (2010) 1765–1778.

[57] X. Peng, M.Q. Zhang, F. Conserva, G. Hosny, G. Selivanova, V.J. Bykov, et al., APR-246/PRIMA-1MET inhibits thioredoxin reductase 1 and converts the enzyme to a dedicated NADPH oxidase, Cell Death Dis. 4 (2013) e881.

[58] D. Volonte, F. Galbiati, Inhibition of thioredoxin reductase 1 by caveolin 1 promotes stress-induced premature senescence, EMBO Rep. 10 (12) (2009) 1334–1340.

[59] B.M. Collins, M.J. Davis, J.F. Hancock, R.G. Parton, Structure-based reassessment of the caveolin signaling model: do caveolae regulate signaling through caveolin-protein interactions? Dev. Cell 23 (1) (2012) 11–20.

[60] M. Bucci, J.P. Gratton, R.D. Rudic, L. Acevedo, F. Roviezzo, G. Cirino, et al., In vivo delivery of the caveolin-1 scaffolding domain inhibits nitric oxide synthesis and reduces inflammation, Nat. Med. 6 (12) (2000) 1362–1367.

[61] J.P. Gratton, M.I. Lin, J. Yu, E.D. Weiss, Z.L. Jiang, T.A. Fairchild, et al., Selective inhibition of tumor microvascular permeability by cavtratin blocks tumor progression in mice, Cancer Cell 4 (1) (2003) 31–39.

[62] A.S. Marudamuthu, Y.P. Bhandary, L. Fan, V. Radhakrishnan, B. MacKenzie, E. Maier, et al., Caveolin-1-derived peptide limits development of pulmonary fibrosis, Sci. Transl. Med. 11 (522) (2019).

[63] V. Gopu, L. Fan, R.S. Shetty, M.R. Nagaraja, S. Shetty, Caveolin-1 scaffolding domain peptide regulates glucose metabolism in lung fibrosis, JCI Insight 5 (19) (2020).

[64] F.D. Johnson, J. Ferrarone, A. Liu, C. Brandstadter, R. Munuganti, D.A. Farnsworth, et al., Characterization of a small molecule inhibitor of disulfide reductases that induces oxidative stress and lethality in lung cancer cells, Cell Rep. 38 (6) (2022) 110343.

[65] L. Zhong, E.S. Arner, J. Ljung, F. Aslund, A. Holmgren, Rat and calf thioredoxin reductase are homologous to glutathione reductase with a carboxyl-terminal elongation containing a conserved catalytically active penultimate selenocysteine residue, J. Biol. Chem. 273 (15) (1998) 8581–8591.

[66] S.Y. Liu, T.C. Stadtman, Heparin-binding properties of selenium-containing thioredoxin reductase from HeLa cells and human lung adenocarcinoma cells, Proc. Natl. Acad. Sci. U. S. A. 94 (12) (1997) 6138–6141.

[67] N. Shu, L.G. Lorentzen, M.J. Davies, Reaction of quinones with proteins: kinetics of adduct formation, effects on enzymatic activity and protein structure, and potential reversibility of modifications, Free Radic. Biol. Med. 137 (2019) 169–180.

[68] A.B. Witte, K. Anestal, E. Jerremalm, H. Ehrsson, E.S.J. Arnér, Inhibition of thioredoxin reductase but not of glutathione reductase by the major classes of alkylating and platinum-containing anticancer compounds, Free Radic. Biol. Med. 39 (5) (2005) 696–703.

[69] R.G. Parton, Caveolae: structure, function, and relationship to disease, Annu. Rev. Cell Dev. Biol. 34 (2018) 111–136.

[70] R.G. Parton, M.A. Del Pozo, S. Vassilopoulos, I.R. Nabi, S. Le Lay, R. Lundmark, et al., Caveolae: the FAQs, Traffic 21 (1) (2020) 181–185.

[71] Y. Wu, Y.W. Lim, D.A. Stroud, N. Martel, T.E. Hall, H.P. Lo, et al., Caveolae sense oxidative stress through membrane lipid peroxidation and cytosolic release of CAVIN1 to regulate NRF2, Dev. Cell 58 (5) (2023) 376–397 e4.

[72] M. Cebula, N. Moolla, A. Capovilla, E.S.J. Arnér, The rare TXNRD1_v3 ("v3") splice variant of human thioredoxin reductase 1 protein is targeted to membrane rafts by N-acylation and induces filopodia independently of its redox active site integrity, J. Biol. Chem. 288 (14) (2013) 10002–10011.

[73] J.D. Hayes, A.T. Dinkova-Kostova, K.D. Tew, Oxidative stress in cancer, Cancer Cell 38 (2) (2020) 167–197.

[74] J. Zhang, X. Li, X. Han, R. Liu, J. Fang, Targeting the thioredoxin system for cancer therapy, Trends Pharmacol. Sci. 38 (9) (2017) 794–808.

[75] R. Gencheva, E.S.J. Arnér, Thioredoxin reductase inhibition for cancer therapy, Annu. Rev. Pharmacol. Toxicol. (2021).

[76] P.K. Mandal, M. Schneider, P. Kolle, P. Kuhlencordt, H. Forster, H. Beck, et al., Loss of thioredoxin reductase 1 renders tumors highly susceptible to pharmacologic glutathione deprivation, Cancer Res. 70 (22) (2010) 9505–9514.

[77] P.K. Mandal, A. Seiler, T. Perisic, P. Kolle, A. Banjac Canak, H. Forster, et al., System x(c)- and thioredoxin reductase 1 cooperatively rescue glutathione deficiency, J. Biol. Chem. 285 (29) (2010) 22244–22253.

[78] R. Somwar, D. Shum, H. Djaballah, H. Varmus, Identification and preliminary characterization of novel small molecules that inhibit growth of human lung adenocarcinoma cells, J. Biomol. Screen 14 (10) (2009) 1176–1184.

[79] M. Liu, S. Sun, Y. Meng, L. Wang, H. Liu, W. Shi, et al., Benzophenanthridine alkaloid chelerythrine elicits necroptosis of gastric cancer cells via selective conjugation at the redox hyperreactive C-terminal sec(498) residue of cytosolic selenoprotein thioredoxin reductase, Molecules 28 (19) (2023).

[80] Z. Xu, J. Xu, S. Sun, W. Lin, Y. Li, Q. Lu, et al., Mecheliolide elicits ROS-mediated ERS driven immunogenic cell death in hepatocellular carcinoma, Redox Biol. 54 (2022) 102351.

[81] E.J. Ste Marie, R.J. Wehrle, D.J. Haupt, N.B. Wood, A. van der Vliet, M.J. Previs, et al., Can selenoenzymes resist electrophilic modification? Evidence from thioredoxin reductase and a mutant containing alpha-methylselenocysteine, Biochemistry 59 (36) (2020) 3300–3315.

[82] X. Chen, S. Sun, S. Huang, H. Yang, Q. Ye, L. Lv, et al., Gold(I) selenium N-heterocyclic carbene complexes as potent antibacterial agents against multidrug-resistant gram-negative bacteria via inhibiting thioredoxin reductase, Redox Biol. 60 (2023) 102621.

[83] S. Sun, W. Xu, H. Zhou, Y. Zhang, J. Zhang, X. Li, et al., Efficient purification of selenoprotein thioredoxin reductase 1 by using chelating reagents to protect the affinity resins and rescue the enzyme activities, Process Biochem. 101 (2021) 256–265.

[84] Y. Yang, S. Sun, W. Xu, Y. Zhang, R. Yang, K. Ma, et al., Piperlongumine inhibits thioredoxin reductase 1 by targeting selenocysteine residues and sensitizes cancer cells to erastin, Antioxidants 11 (4) (2022) 710.

[85] S. Sun, Y. Zhang, W. Xu, Y. Zhang, R. Yang, J. Guo, et al., Chlorophyllin inhibits mammalian thioredoxin reductase 1 and triggers cancer cell death, Antioxidants 10 (11) (2021) 1733.

[86] H. Wang, S. Sun, Y. Ren, R. Yang, J. Guo, Y. Zong, et al., Selenite ameliorates cadmium-induced cytotoxicity through downregulation of ROS levels and upregulation of selenoprotein thioredoxin reductase 1 in SH-SY5Y cells, Biol. Trace Elem. Res. 201 (1) (2023) 139–148.